Journal of Solid State Chemistry **154,** 603–611 (2000)
doi:10.1006/jssc.2000.8902, available online at http://www.idealibrary.com on IDEAL®

Reversible Antifluorite to Anticotunnite Phase Transition in Li_2S at High Pressures

A. Grzechnik,*[,1] A. Vegas,*[,†] K. Syassen,* I. Loa,* M. Hanfland,[‡] and M. Jansen*

*Max-Planck-Institut für Festkörperforschung, Heisenbergstrasse 1, D-70569 Stuttgart, Germany; †Instituto de Quimica Fisica "Rocasolano," CSIC, Serrano 119, E-28006 Madrid, Spain; and ‡European Synchrotron Radiation Facility, B.P. 220, F-38000 Grenoble, France

Received May 23, 2000; in revised form July 6, 2000; accepted July 28, 2000; published online September 30, 2000

We have investigated the high-pressure behavior of lithium sulfide Li_2S by Raman spectroscopy and synchrotron angle-dispersive powder X-ray diffraction in a diamond anvil cell ($T = 298$ K). There occurs a fully reversible phase transition from the antifluorite ($Fm3m$, $Z = 4$) to an orthorhombic structure at about 12 GPa (increasing pressure). Atomic positions of the orthorhombic phase were refined using the Rietveld method. Near 20 GPa the structure of the high pressure phase is of the anticotunnite type ($Pnma$, $Z = 4$), which consists of a distorted hexagonal close packed (hcp) array of S atoms, Li(1) atoms occupying all the octahedral sites, and Li(2) atoms situated in one-half of the tetrahedral positions. The Li(1) atoms are shifted toward one of the S atoms so that their actual coordination is square pyramidal (5 + 1). At lower pressures the orthorhombic phase passes through an intermediate structural arrangement where the Li atoms are disordered, occupying a larger fraction of the tetrahedral sites of the anticotunnite-like *hcp* sulfur sublattice. Based on the analysis of atomic positions, we discuss the mechanism for the antiflourite to anticotunnite transformation.

INTRODUCTION

Lithium sulfide Li_2S, first synthesized by Zintl *et al.* (1), has the antifluorite structure at ambient conditions, $Fm3m$, $Z = 4$ (1, 2). It undergoes a diffuse ("Faraday") phase transition to a fast-ion-conduction region at about 850 K and is referred to as a superionic conductor (3, 4). Its high ionic conductivity is discussed as a consequence of a Frenkel defect formation by a lithium atom redistribution on their regular sites as well as on interstitial sites without any significant distortion of the fcc sulfur sublattice.

Pressure-induced phase transitions in the *fluorite* compounds into the $PbCl_2$ (cotunnite) structure ($Pnma$, $Z = 4$) were first reported for CaF_2, SrF_2, BaF_2, PbF_2, and EuF_2 (5, 6). The orthorhombic structures of CaF_2 and BaF_2 were refined from X-ray and neutron diffraction data by Gerward *et al.* (7) and by Leger *et al.* (8), respectively. Subsequently, the same fluorite → cotunnite transition was found to take place in several dihalogenides and dioxides (9–11). Some of the dihalogenides further transform into the "post" cotunnite ($P2_1/a$, $Z = 8$) or Ni_2In ($P6_3/mmc$, $Z = 2$) structures (12). The sequence of pressure-induced transitions $Fm3m \rightarrow Pnma \rightarrow P2_1/a$ or $Fm3m \rightarrow Pnma \rightarrow P6_3/mmc$ involves an increase of the cation coordination numbers from 8 (fluorite), 9 (cotunnite), and 10 ("post" cotunnite) to 11 (Ni_2In).

The first reported studies of pressure-induced structural changes in the *antifluorite* compounds concern Mg_2Si, Mg_2Ge, and Mg_2Sn (13, 14). In these materials, phase transitions were observed in the range from 2.5 to 5.5 GPa and the powder diffraction patterns of the high-pressure phases were indexed on the basis of a hexagonal cell. However, two more recent studies carried out on Mg_2Ge and Mg_2Sn showed that these hexagonal phases do not correspond to compounds with the ideal 2:1 stoichiometry but to compositions Mg_9Sn_5 (15) and Mg_2Sn_{1+x} (16), respectively. In the former, the crystal structure determination revealed that the Mg subarray is very similar to that of the cotunnite structure, the small differences being a result of an insertion of additional Sn atoms (15). In the latter, the satellite reflections were interpreted as due to the existence of a composite with two closely related crystal structures corresponding to two incommensurate atomic subsystems (16).

In this study, we are interested in the high pressure behavior of lithium sulfide at room temperature. Structure and properties of this material have so far been extensively studied as a function of temperature at atmospheric conditions but not as a function of elevated pressures. Here, we present our high-pressure data on Li_2S obtained by *in situ* Raman spectroscopy and angle-dispersive X-ray diffraction in a diamond anvil cell at pressures up to 20 GPa ($T = 298$ K).

[1] To whom correspondence should be addressed. Fax: ++49 711 689 1444. E-mail: andrzej@servix.mpi-stuttgart.mpg.de.

0022-4596/00 $35.00

EXPERIMENTAL

A finely grained sample of Li_2S (Alfa-Aesar) with the 99.9% nominal purity was used for all the experiments. A chemical analysis of the compound with the ICP method gave the stoichiometry $Li_{1.975}S$. The deviation from the ideal composition is within the error limits of the analytical technique. Small amounts of oxygen which could be due to the presence of impurities of Li_2SO_4 were detected. However, these impurities could not be observed by X-ray diffraction and Raman spectroscopy so that in all the subsequent experimental procedures and data analysis we assumed that our sample has the ideal Li_2S stoichiometry. The X-ray powder diffraction diagram at ambient pressure was obtained with a STOE diffractometer in the 2θ range of $10-85^\circ$ using monochromatic Cu$K\alpha_1$ radiation. A least-squares refinement of the 2θ values for nine reflexions of Li_2S, with silicon as an internal standard, led to the unit cell parameter $a = 5.7125$ (2) Å.

Both the high-pressure Raman and the XRD experiments up to 20 GPa ($T = 298$ K) were carried out on the same batch of the sample. The Li_2S fine powder was always handled in glove boxes. It was loaded into diamond cells (DACs) without any pressure medium. Raman spectra were collected using a triple spectrograph with CCD signal detection. Raman scattering was excited using an Ar ion laser at a wavelength of 487.98 nm. Angle-dispersive X-ray powder diffractograms in a DAC were measured on the ID9 beamline at the European Synchrotron Radiation Facility (Grenoble). Monochromatic radiation at $\lambda = 0.43171(1)$ Å was used for pattern collection on image plates. The images were integrated using the program FIT2D (17) to yield intensity versus 2θ diagrams. The instrumental resolution (the minimum full width at half height of diffraction peaks) was about 0.03°. To improve powder averaging, the DAC was rotated by $\pm 3^\circ$. The ruby fluorescence method (18) was used for pressure calibration.

RESULTS

Raman Spectroscopy

At ambient pressure, only one Raman mode of the F_{2g} symmetry, mainly due to the motion of the Li sublattice, is allowed for the cubic antifluorite structure (3, 4). This mode is observed at 372 cm^{-1}. An additional broad and weak band is seen at 462 cm^{-1} (Fig. 1). The frequency of this band approximately agrees with that of a rather flat longitudinal optical (LO) phonon branch as determined by inelastic neutron scattering (3). Thus, the broad Raman feature possibly is due to first-order LO scattering, induced by a small size of crystallites and/or disorder effects. On the other hand, no disorder-induced scattering is observed in

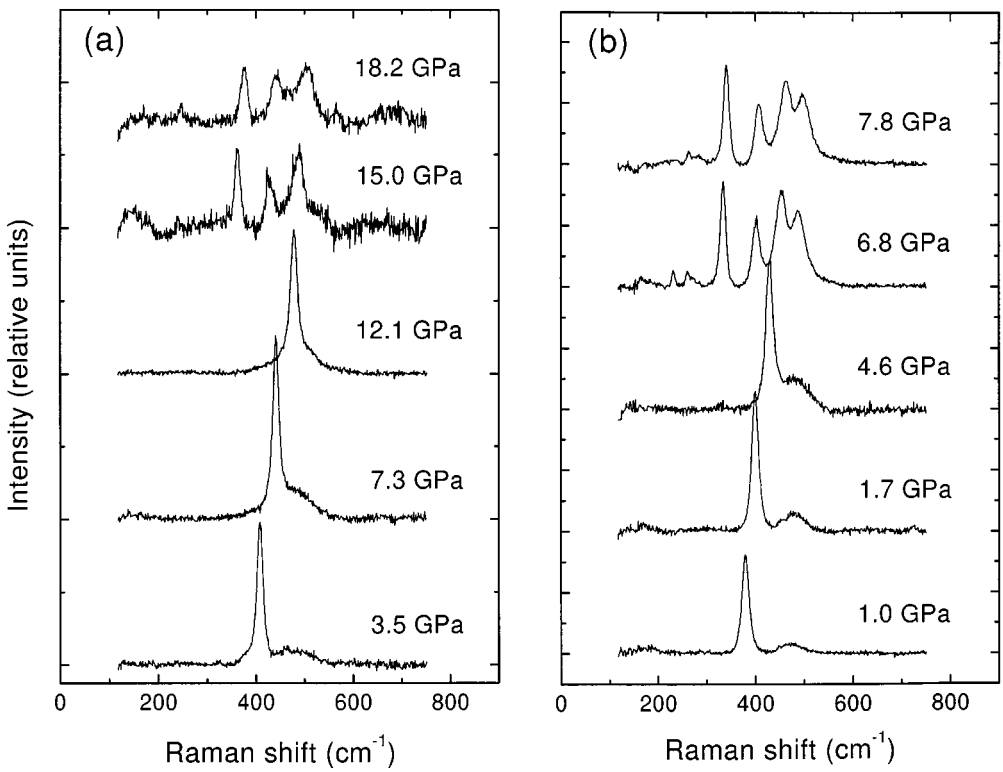

FIG. 1. Raman spectra of Li_2S upon compression (a) and decompression (b).

the acoustical phonon regime. Therefore, we cannot rule out that the broad feature arises from second-order Raman scattering involving zone boundary acoustical modes.

Upon compression (Fig. 1a) both Raman peaks shift to higher energy. At pressures above about 12.5 GPa new Raman bands appear. Furthermore, a significant decrease in intensity of the Raman signal is observed. In transmitted light the sample turns dark yellow. The changes in the Raman peaks indicate a structural phase transition. The hysteresis is significant and the high-pressure phase can be retained down to about 6 GPa, as indicated by the Raman spectra for decreasing pressure shown in Fig. 1b. Upon decompression, the intensity changes in the spectra are reversible. Up to four strong and two weak features can be identified in the Raman spectra of the high pressure phase. This is clearly evident from spectra measured for decreasing pressure (Fig. 1b).

Figure 2 shows Raman frequencies as a function of pressure for the antifluorite phase and the high-pressure modification of Li_2S. We note the rather strong pressure dependence of the F_{2g} mode of the cubic phase. Its shift is about three times larger compared to that of the the broad Raman feature observed for the cubic phase.

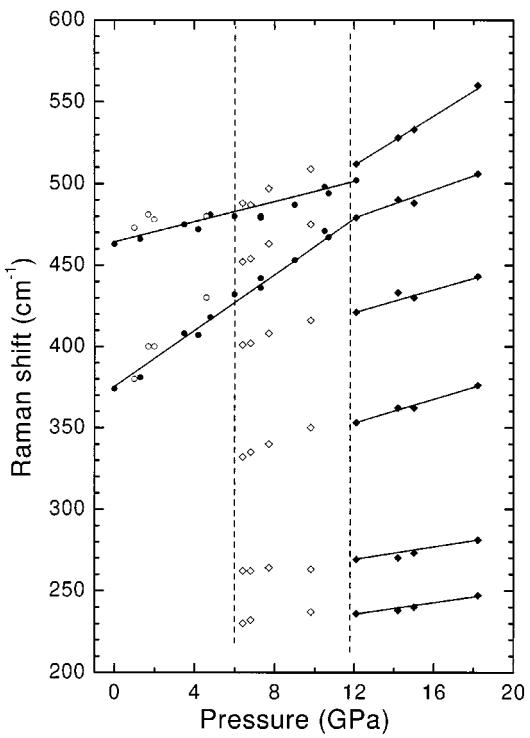

FIG. 2. Pressure shift of the Raman bands of Li_2S. Circles and diamonds refer to the antifluorite (*Fm3m*, $Z = 4$) and orthorhombic (*Pnma*, $Z = 4$) phases, respectively. Solid and open symbols are for increasing and decreasing pressure, respectively. Lines through the data points measured for increasing pressure are guides for the eye. The dashed vertical lines indicate phase transition pressures for increasing and decreasing pressure.

X-Ray Diffraction

Diffraction diagrams measured at different pressures are shown in Fig. 3. At pressures up to about 13 GPa, all the diffraction peaks are due to the cubic antifluorite structure. At higher pressures, additional peaks appear, indicating the onset of a phase transition in agreement with the Raman data. The pressure region upon compression, at which the two phases coexist, is quite broad and the reflections corresponding to Li_2S antifluorite completely disappear at about 18 GPa. The high-pressure polymorph can be decompressed at least down to 7.9 GPa.

All the Bragg peaks of the new phase at 20.5 GPa could be indexed (19) on the basis of only one orthorhombic cell: $a = 5.724(6)$ Å, $b = 3.559$ (4) Å, and $c = 6.669$ (4) Å ($M_{21} = 6.7$, $F_{21} = 15.6$). The cell volume $V = 135.87$ Å^3 indicated that the number of Li_2S formula units in the unit cell is four, $Z = 4$. The systematic extinctions consistent with space group *Pnma* together with the unit cell dimensions suggested that the new orthorhombic phase would have the anticotunnite structure. A full Rietveld profile refinement of the pattern at 18.8 GPa (Fig. 4) was carried out using the program GSAS (20). The starting atomic coordinates were those of the cesium and sulfur atoms in Cs_2S (21). The refined parameters were the fractional coordinates, isotropic thermal parameters, Chebyshev polynomial background, Stephens profile function (22), cell parameters, and March-Dollase correction for preferred orientation. The same strategy and sets of structural and global parameters were used for all the other Rietveld refinements discussed in this work. It should be emphasized that the Stephens profile function, incorporating the anisotropic peak broadening due to a strain (22), is indispensable for the case of the high-pressure experiments with an uniaxial compression component in a DAC. The refinement converged to $R_{wp} = 12.4\%$, $R_p = 10.0\%$, $\chi^2 = 2.47$, $R(F^2) = 8.4\%$. The final atomic and lattice parameters are given in Table 1 and Table 2 lists the interatomic distances. The structure is represented in Fig. 5. The Li(1) atoms occupy half of the available tetrahedral sites. The octahedral Li(2) atoms are shifted from the equatorial plane toward one of the apical S atoms, leading to a coordination number 5, corresponding to a square pyramide (5 + 1).

Close examination of the patterns collected upon decompression reveals that the relative intensities of the peaks, especially the ones in the range $2\theta = 7.5$–$9°$, are continuously changing (Figs. 3 and 4). For instance, there is an intensity inversion of the (011) and (111) reflections at 7.9 GPa relative to the intensity ratio of these peaks at much higher pressures. Indexing all the patterns upon decompression can be done using the orthorhombic cell (*Pnma*, $Z = 4$) and there are no peaks (dis)appearing that would possibly suggest changes in symmetry. However, a Rietveld refinement of the pattern at 7.9 GPa with the anticotunnite structure

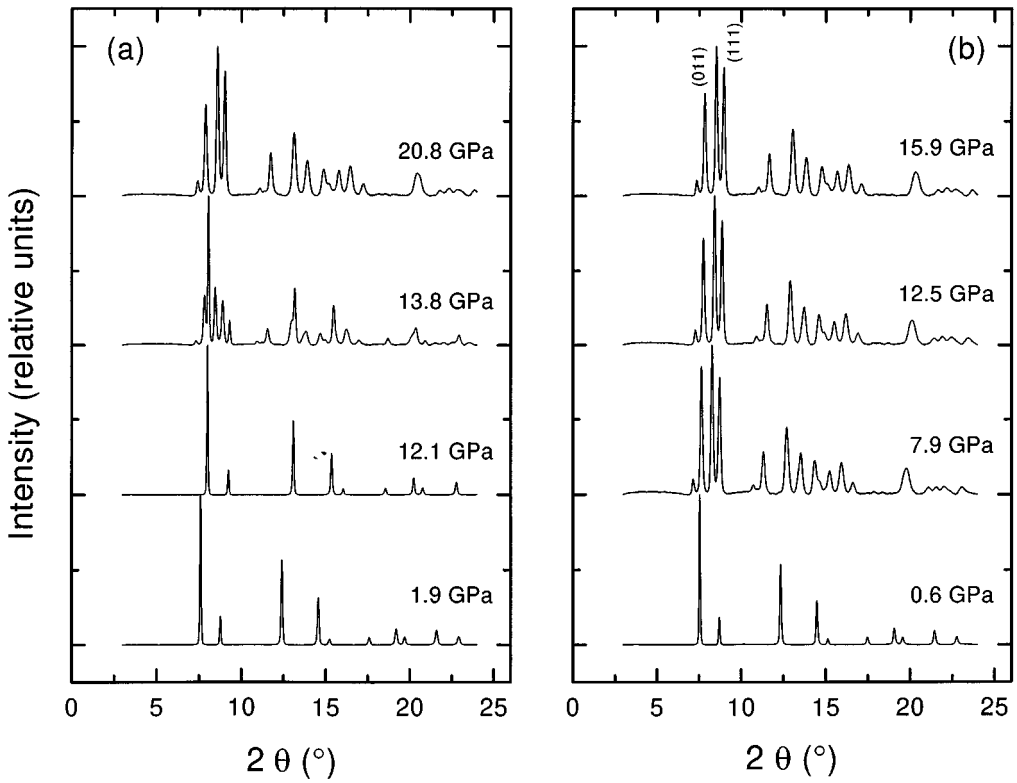

FIG. 3. X-ray powder diffraction patterns of Li_2S upon compression (a) and decompression (b). Miller indices are given for the (011) and (111) reflections of the high-pressure orthorhombic phase.

failed with unacceptably short Li–S bonds. When constraints on the minimal Li–S and Li–Li distances were used, such "soft" constraints could not be removed at any stage of the refinement. Additionally, the relative contribution of these constraints to χ^2 at the final stage amounted to 97% and the R agreement factors were very poor. It should be noted that similar intensity anomalies are observed upon compression just above the phase transition in the region where the two phases coexist (Fig. 3). We thus attribute the intensity changes of Bragg peaks observed upon applying/releasing pressure to a rearrangement of Li atoms within the sulfur framework.

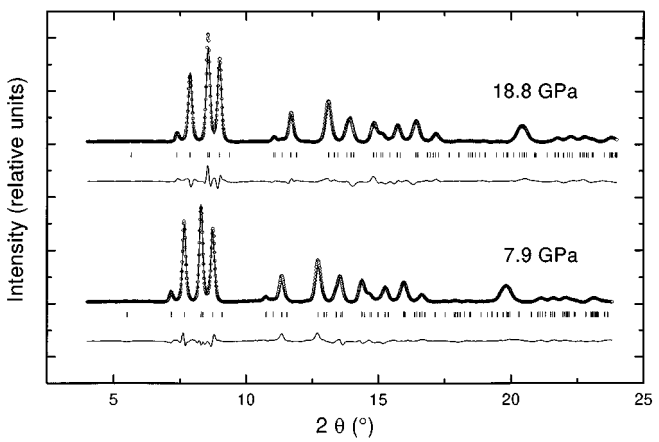

FIG. 4. Observed, calculated, and difference X-ray diffraction profiles of orthorhombic Li_2S at 18.8 GPa (increasing pressure) and 7.9 GPa (decreasing pressue). Vertical markers indicate Bragg reflections.

Application of direct methods (23) to solve the structure of Li_2S in the *Pnma* space group from the pattern at 7.9 GPa yields 5 maxima in the Fourier maps, all of them at the special positions $4c$ $(x, \frac{1}{4}, y)$ (Table 3). The highest maximum corresponds to the S atom at the coordinates close to those of the anticotunnite structure. The remaining four maxima are approximately of the same height. Two of them reproduce, together with the S atom, the anticotunnite structure

TABLE 1
Final Atomic Coordinates for the Anticotunnite Phase of Li_2S at 18.8 GPa—*Pnma* ($Z = 4$), $a = 5.7353(11)$ Å, $b = 3.5448(4)$ Å, $c = 6.6861(8)$ Å

	x	y	z
S	0.7559(9)	$\frac{1}{4}$	0.6075(2)
Li(1)	0.1535(20)	$\frac{1}{4}$	0.5735(16)
Li(2)	0.500(5)	$\frac{1}{4}$	0.3210(18)

TABLE 2
Interatomic Distances (Å) in the Coordination Polyhedra around Li Atoms in the Anticotunnite Phase of Li_2S at 18.8 GPa

$Li(1)S_4$ tetrahedron		$Li(2)S_6$ octahedron	
Li(1)–S^{ii}	2.296(12)	Li(2)–S^{iii}	2.351(17)
–S^{iii}	2.216(11)	–S^{iv}	2.351(17)
–S^{iv}	2.212(7)	–S^{vi}	2.680(16)
–S^{v}	2.212(7)	–S^{vii}	2.680(16)
		–S^{i}	2.420(19)
		–S^{viii}	3.192(16)

Note. Symmetry codes: i, x, y, z; ii, $x-1, y, z$; iii, $x-\frac{1}{2}, y, \frac{3}{2}-z$; iv, $1-x, y, 1-z$; v, $1-x, y+\frac{1}{2}, 1-z$; vi, $\frac{3}{2}-x, y, z-\frac{1}{2}$; vii, $\frac{3}{2}-x, y+\frac{1}{2}, z-\frac{1}{2}$; viii, $x-\frac{1}{2}, y, \frac{1}{2}-z$.

TABLE 3
Atomic and Fourier Peak Coordinates for Li_2S (*Pnma*, $Z=4$) at 7.9 GPa Obtained with Direct Methods (23)

	Height	x	y	z
S	2210	0.774	$\frac{1}{4}$	0.604
Li_c	269	0.090	$\frac{1}{4}$	0.596
Li_c	224	0.470	$\frac{1}{4}$	0.573
Li	217	0.935	$\frac{1}{4}$	0.372
Li	200	0.215	$\frac{1}{4}$	0.614

Note. The final $R(F^2)$ value of a calculated diffraction pattern using all five atoms and half-occupancy of Li sites, with no Rietveld refinement, is 12.3%. The two atoms Li_c, together with the sulfur atom, give the anticotunnite structure displaced by the vector $c/2$.

displaced by $c/2$. The other two and the S atom form a new arrangement, discussed below. A calculated diffractogram with all five atom positions and half-occupancy of the Li sites accounts very well for the inversion of the intensities. However, a determination of interatomic distances results in some very short (well below 2 Å) Li–S and Li–Li distances.

The results given in Table 3 suggest a structural model where a mixture of two phases is assumed, i.e., an anticotunnite phase and a second component, that has the same lattice parameters and the same structural parameters for the sulfur sublattice, but a different arrangement of Li atoms. In our two-phase refinements described below, the "soft" constraints for atomic distances in both phases were necessary only in the initial stages and could be removed for the final refinement. In the first case considered, both components have the *Pnma* symmetry and all the atoms occupy the 4*c* sites ($x, \frac{1}{4}, z$) in the *Pnma* lattice. After the refinement, however, some of the Li–Li and Li–S distances in the second (non-anticotunnite) component were found to be anomalously short, and the model was rejected.

We thus considered a second case where the anticotunnite component has the *Pnma* space group, while the other phase is in the $Pn2_1a$ space group and both components have equal abundance. The noncentrosymmetric space group allows for a higher degree of freedom in the lithium atom positions. In the space group $Pn2_1a$, which has the same extinction conditions as *Pnma*, these atoms are in the general 4*a* sites (x, y, z) with no restriction $y=\frac{1}{4}$. The refined structural model with the second component in the $Pn2_1a$ space group is given in Table 4. The origin of the unit cell in the $Pn2_1a$ space group was fixed at the sulfur atoms by restraining their y coordinate at $y=\frac{1}{4}$. The optimized

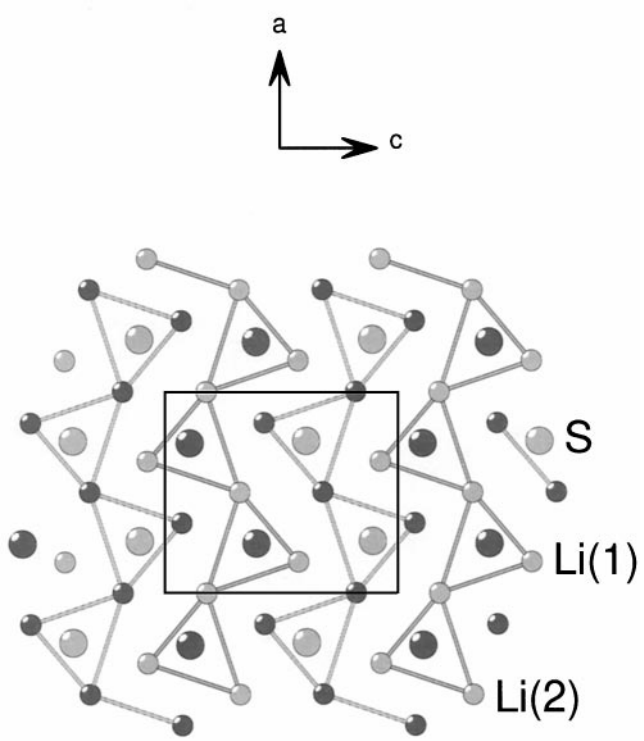

FIG. 5. Crystal structure of anticotunnite Li_2S at 18.8 GPa (*Pnma*, $Z=4$). Large and small circles are the sulfur and lithium atoms, respectively. Dark and light symbols stand for the atoms at $y=\frac{3}{4}$ and $y=\frac{1}{4}$, respectively.

TABLE 4
Final Atomic Coordinates for Orthorhombic Li_2S at 7.9 GPa

	x	y	z
Pnma ($Z=4$)			
S	0.7700(7)	$\frac{1}{4}$	0.6077(12)
Li(1)	0.9298(20)	$\frac{1}{4}$	0.3633(17)
Li(2)	0.315(3)	$\frac{1}{4}$	0.555(3)
$Pn2_1a$ ($Z=4$)			
S	0.7700(7)	$\frac{1}{4}$	0.6077(12)
Li(1)	0.849(2)	0.78(2)	0.362(2)
Li(2)	0.522(3)	0.797(14)	0.406(3)

Note. The cell parameters are $a=5.9219(13)$ Å, $b=3.6463(4)$ Å, $c=6.8977(8)$ Å. The results refer to a two-phase refinement involving equal weights of the *Pnma* and $Pn2_1a$ components.

TABLE 5
Interatomic Li–S Distances (Å) in the $Pn2_1a$ Phase of Li_2S at 7.9 GPa

$Li(1)S_4$ tetrahedron		$Li(2)S_4$ tetrahedron	
Li(1)–S^{i}	2.60(7)	Li(2)–S^{i}	2.84(4)
–S^{ii}	2.46(6)	–S^{ii}	2.61(4)
–S^{iii}	1.89(2)	–S^{iii}	2.41(2)
–S^{iv}	2.27(2)	–S^{v}	1.74(2)
Distances in the Li–wurtzite-like net			
Li(1)–$Li(1)^{iv}$	3.18(3)	Li(2)–$Li(2)^{viii}$	2.25(2)
–$Li(1)^{vi}$	3.18(3)	–$Li(2)^{v}$	2.25(2)
–$Li(2)^{vii}$	2.12(2)	–$Li(1)^{ix}$	2.12(2)
–$Li(2)^{i}$	1.97(2)	–$Li(1)^{i}$	1.97(2)

Note. Symmetry codes: i, x, y, z; ii, $x, 1+y, z$; iii, $\frac{3}{2}-x, \frac{1}{2}+y, z-\frac{1}{2}$; iv, $2-x, \frac{1}{2}+y, 1-z$; v, $1-x, \frac{1}{2}+y, 1-z$; vi, $2-x, y-\frac{1}{2}, 1-z$; vii, $\frac{1}{2}+x, y, \frac{1}{2}-z$; viii, $1-x, y-\frac{1}{2}, 1-z$; ix, $x-\frac{1}{2}, y, \frac{1}{2}-z$.

y coordinate for the Li(1) atom is close to $y=\frac{3}{4}$. The refinement converged to $R_{wp}=12.9\%$, $R_p=10.1\%$, $\chi^2=2.76$, $R(F^2)=12.0\%$ (Fig. 4). The final interatomic distances are collected in Table 5. The major feature of the atomic arrangement in the $Pn2_1a$ component, discussed in more detail in the next section, is the presence of empty octahedral positions and the occurrence of all the Li atoms at two adjacent tetrahedral sites; i.e., the two coordination tetrahedra of Li have a common face. From a stereochemical point of view (a Pauling rule), such an arrangement may be considered unstable as a result of the Li–Li repulsion. On the other hand, all determined Li–Li and Li–S distances are comparable to the ones found in other Li-containing compounds at ambient pressure, e.g., $Li_4Mo_6S_8$ (Li–Li = 2.09, 2.13 Å) (24), Li_3InO_3 (Li–Li = 1.96–2.33 Å) (25), $Li_8O_2(GeO_4)$ (Li–Li = 2.19 Å) (26), Li_8CoO_6 (Li–Li = 2.13 Å) (27), $Li_{1.02}Mo_6S_8$ (Li–S = 2.00 Å) (24), and $Li_4Re_6S_{11}$ (Li–S = 2.08 Å) (28).

We tested a third model that is based on the parent anticotunnite structure (Fig. 5). In this model, the Li atoms at the octahedral sites would be distributed at two split positions shifted toward the opposite apical sulfur atoms; i.e., the actual coordination for the two split sites would be 5 + 1. This, in turn, would give very short Li–Li distances with the lithium atoms occupying the half of tetrahedral sites. To avoid this situation, lithium atoms would need to be distributed over the available tetrahedral positions in a correlated manner. Such a cooperative redistribution of the Li atoms leads to two interpenetrating structures displaced with respect to each other by a vector $c/2$. A Rietveld refinement with this set of tetrahedral and octahedral sites, fixed at 0.5 each, converged to $R(F^2)=13.0\%$. When the respective split occupancies were refined, this agreement factor dropped to 10.9%. Like in the previous two-phase model, all determined Li–Li and Li–S distances fall in an acceptable range. However, the inversion of the intensities of the (011) and (111) peaks is not well accounted for.

From our structural modeling of the low-pressure diffraction data of orthorhombic Li_2S we conclude that a two-phase model involving equal abundance of an anticotunnite component and a second component with $Pn2_1a$ space group provides the most satisfactory, but still approximate, description of the disordered arrangement of Li atoms which develops in the low-pressure regime of the orthorhombic phase. At higher pressure the disorder is reduced, such that near 20 GPa we arrive at the anticotunnite structure, where all octahedral sites and half of the tetrahedral sites are occupied.

Equation of State and Grüneisen Parameters

The pressure dependence of lattice parameters and unit cell volume is shown in Fig. 6. The unit cell volume of the antifluorite phase, determined from the X-ray pattern collected at ambient pressure, is 186.41 Å^3. The relative volume change for the antifluorite and orthorhombic phases of Li_2S at 13.7 GPa is 6.6%. The third-order Birch-Murnaghan equation of state (29) was used for fitting the pressure dependences of the unit cell volume. The extracted isothermal bulk modulus (K_0), and its first derivative (K_0'), both at zero pressure, for the antifluorite phase are 52(2) GPa and 2.1(4), respectively. The corresponding parameters for the orthorhombic polymorph at $V_0=141$ Å^3 ($P_0=13.6$ GPa) are $K_0=137(23)$ GPa and $K_0'=4$ (fixed). The sensitivity of the sample precluded a use of any pressure medium. However, we would like to point out that Li_2S, especially in the antifluorite structure, is relatively soft so that the obtained values of the bulk moduli as well as the accuracies of transition pressure for both the Raman and X-ray data are not significantly affected by nonhydrostatic conditions of our experiments.

The volume dependence of Raman modes can be described by a mode Grüneisen parameter $\gamma=-(\partial \ln \nu/\partial \ln V)=(K_0/\nu_0)\ (\partial \nu/\partial P)$, where ν is the frequency of a Raman band and V is the volume. For the allowed Raman mode of the antiflurite phase the Grüneisen parameter, assuming $K_0=52$ GPa, is $\gamma=1.26$. For the broad Raman feature observed in the antifluorite phase we have $\gamma=0.35$. The Grüneisen parameters for the Raman features of the orthorhombic phase, corresponding to the slopes of the solid lines in Fig. 2, range from about $\gamma=1.5$ to $\gamma=3.0$.

DISCUSSION

The results of this study show that at room temperature lithium sulfide undergoes a pressure-induced antifluorite → anticotunnite phase transition at about 12 GPa. In this respect, Li_2S behaves like fluorite-type compounds, which transform to their cotunnite-type polymorphs at high pressures (5–12). For the antifluorite-structured light alkali

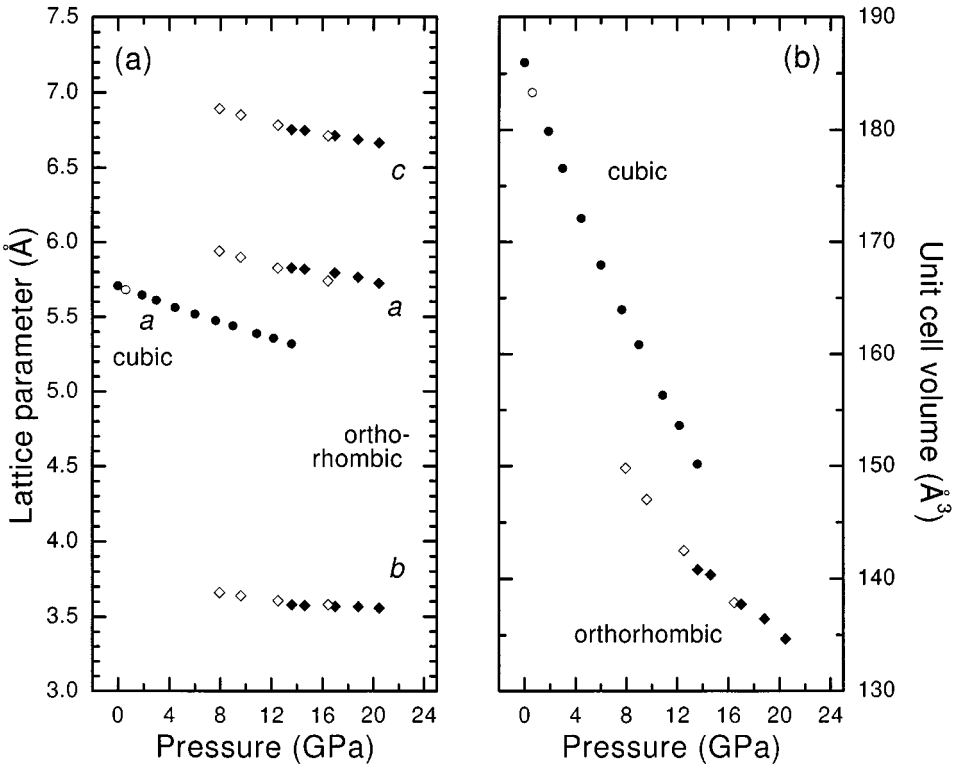

FIG. 6. Pressure dependence of lattice parameters (a) and unit cell volume (b) of Li_2S. Circles and diamonds refer to the antifluorite and orthorhombic phases, respectively. For both phases the number of formula units in the unit cell is $Z = 4$. Solid and open symbols are for increasing and decreasing pressure, respectively.

metal sulfides this transition is expected, because Cs_2S has the anticotunnite lattice at atmospheric pressure (21). The transformation anticotunnite $\leftrightarrow$ antifluorite in Li_2S involves an orthorhombic intermediate with a disordered lithium sublattice. This disorder is manifested by the anomalous relative intensities of the (011) and (111) X-ray reflections.

The anticotunnite structure (*Pnma*, $Z = 4$) can be described in two different ways. The first one (30–32) considers the coordination polyhedra of the majority element (in this case lithium) around the minority (in this case sulfur) atoms (Fig. 5). Accordingly, the anticotunnite lattice in Li_2S consists of chains of trigonal prisms around the S atoms, connected by common edges and running parallel to the *ab* plane. The chains are displaced by $b/2$ with respect to each other. The S atoms are inserted into these trigonal prisms in such a way that each S^{2-} anion ($y = \frac{1}{4}$) is surrounded by nine Li^+ cations. Six of them ($y = -\frac{1}{4}$ and $\frac{3}{4}$) are situated at the apices of the trigonal prisms and the remaining three ($y = \frac{1}{4}$) belong to adjacent chains and are capping the three lateral faces of the prisms. The interatomic distances given in Table 3 compare well to those expected from the corresponding ionic radii.

An alternative description of this structure has been proposed for Cs_2S (21). The lattice consists of a distorted hcp array of S atoms, with Li(1) atoms occupying all the octahedral sites and Li(2) situated in one-half of the tetrahedral holes (Fig. 5). The octahedral Li atoms are shifted from the equatorial plane toward one of the apical S atoms, leading to a coordination number 5, corresponding to a square pyramide (5 + 1).

The latter description makes it possible to relate the anticotunnite structure to the lithium disorder. From the stereochemical point of view, the disordering could be best explained by the presence of the split octahedral (the actual 5 + 1 coordination) and tetrahedral sites for the lithium atoms. However, the observed X-ray intensity anomalies cannot be well accounted for with such a structure model. The model, whose calculated patterns better match the observed ones, would require a transfer of octahedral Li atoms to the other half of the tetrahedral holes which are empty in the parent anticotunnite lattice. The final (hypothetical) result of such a transfer would be an unaltered hcp arrangement of S atoms with all the tetrahedral sites occupied by Li atoms and with all the octahedral positions unoccupied (Fig. 7).

In such a structure, which is only partially realized in orthorhombic Li_2S, the coordination numbers are again those of the antifluorite type. The S atoms are coordinated by eight Li atoms, forming trigonal prisms, whose triangular

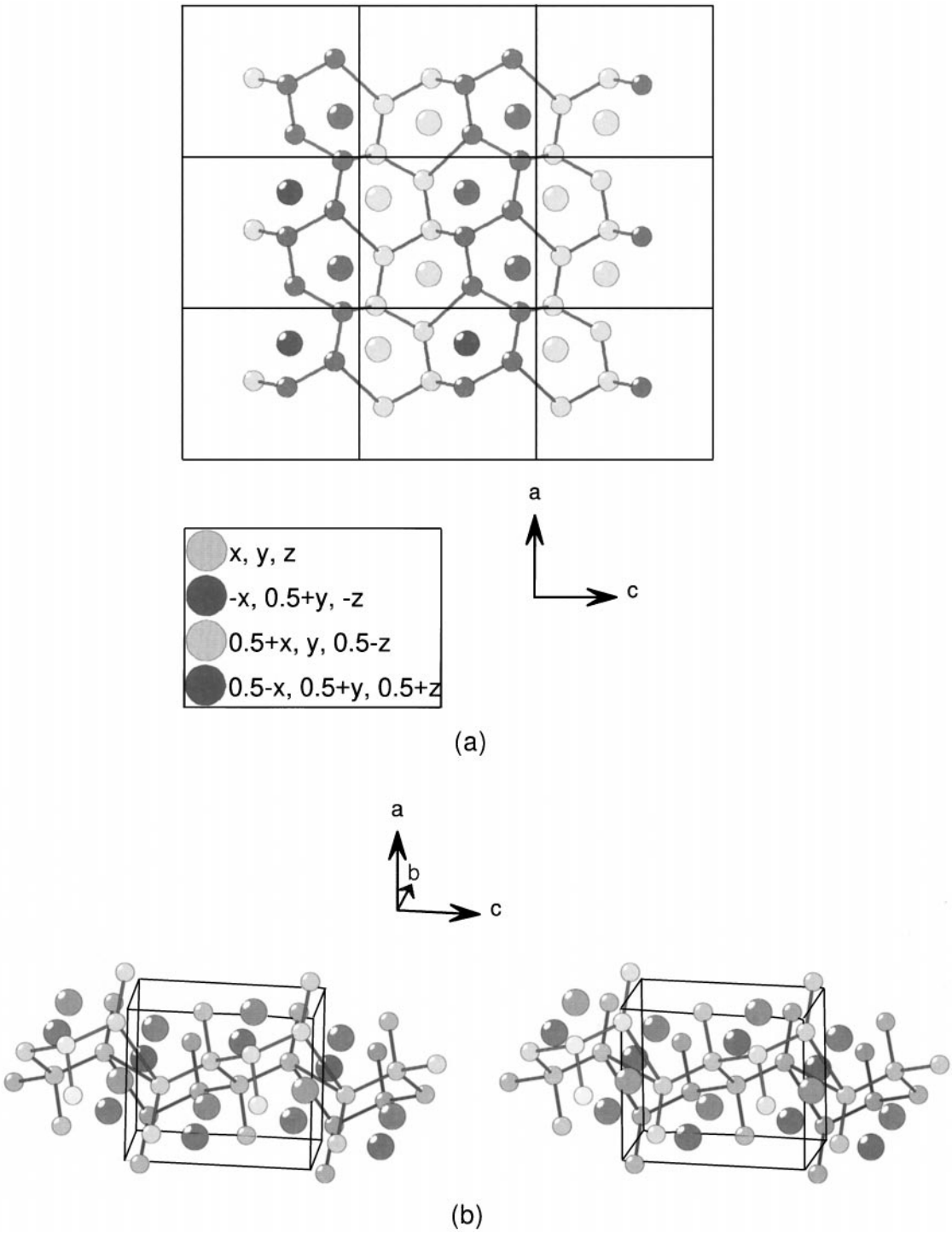

FIG. 7. The intermediate structure of Li_2S in the $Pn2_1a$ space group. (a) A projection along the *b* axis showing the array of the Li atoms. (b) A stereopair showing one layer of chair-conformed hexagons of Li atoms. Large and small circles correspond to S and Li atoms, respectively. Different shades of gray are used for the sake of the oclarity of the stereopair. The mechanism for a formation of the simple cubic subarray of Li atoms can easily be deduced by moving the Li atoms, which form the vertical bonds, above and below the center of the hexagons.

faces are capped by two additional Li atoms. The Li atoms form a tetrahedral wurtzite-like array, in which every Li atom is coordinated by four other ones at distances of 2.11, 2.32, and 2×2.64 Å (Table 5). It should be recalled that in the hcp array, pairs of tetrahedra have a common face. In the $Pn2_1a$ framework (Tables 4 and 5), all these tetrahedra

are occupied by Li atoms separated by the shortest Li–Li distance of 2.11 Å. The Li–Li distance of 2.11 Å would destabilize the lattice as a consequence of the repulsion of the two cations. However, this repulsion could be compensated by the two short Li–S distances (close to 2.00 Å) between the Li atoms and the S atoms at two opposite corners of the tetrahedra (Table 5). In fact, simple Coulomb calculations (21) for the "split Li atom" model and the "all tetrahedral" arrangement reveal that the lattice energies of the two structures (2988 and 3031 kJ/mol at 7.9 GPa, respectively) are very close to each other so that both of them could be expected to occur in the metastability region of the pressure-induced anticotunnite structure, i.e., upon decompression at pressures well below 12 GPa, as well as on compression in the pressure region where the two phases coexist. Lattice expansion on releasing pressure, and hence changes in packing of the sulfur substructure, would result in low-valent lithium atoms occupying a large fraction of the available tetrahedral sites of the hcp lattice.

The structure, with all the octahedral sites unoccupied, can be viewed as a probable intermediate step in the anticotunnite ↔ antifluorite transition. A mechanism for this transition path could be the displacement of every third S layer of the hcp array to form the fcc array present in the antifluorite structure. At the same time the chair-conformed layers of Li atoms, which constitute the wurtzite-like sublattice, are also displaced with respect to each other in such a way that the atoms forming the shortest Li–Li distances are situated above and below the center of every chair-conformed hexagon. The result is a simple cubic net that is in fact the Li sublattice in the antifluorite structure.

ACKNOWLEDGMENT

We thank Christian Schön for several discussions.

REFERENCES

1. E. Zintl, A. Harder, and B. Dauth, *Z. Elektrochem.* **40,** 588 (1934).
2. F. Kubel, B. Bertheville, and H. Bill, *Z. Kristallogr.* **214,** 302 (1999).
3. W. Buehrer, F. Altorfer, J. Mesot, H. Bill, P. Carron, and H. G. Smith, *J. Phys. Condens. Matter* **3,** 1055 (1991).
4. B. Bertheville, H. Bill, and H. Hagemann, *J. Phys. Condens. Matter* **10,** 2155 (1998).
5. K.-F. Seifert, *Fortschr. Miner.* **45,** 214 (1968).
6. D. P. Dandekar and J. C. Jamieson, *Trans. Am. Crystallogr. Assoc.* 19 (1969).
7. L. Gerward, J. Staun Olsen, S. Steenstrup, M. Malinowski, S. Åsbrink, and W. Waskowska, *J. Appl. Crystallogr.* **25,** 578 (1992).
8. J. M. Leger, J. Haines, A. Atouf, O. Schulte, and S. Hull, *Phys. Rev. B* **52,** 13247 (1995).
9. L. H. Brixner, *Mater. Res. Bull.* **11,** 1453 (1976).
10. H. P. Beck, *Z. Anorg. Allg. Chem.* **459,** 72 (1979).
11. S. J. Duclos, Y. K. Vohra, A. L. Ruoff, A. Jayaraman, and G. P. Espinosa, *Phys. Rev. B* **38,** 7755 (1988).
12. J. M. Leger and J. Haines, *Eur. J. Solid State Inorg. Chem.* **34,** 785 (1997).
13. P. Cannon and E. T. Conlin, *Science* **145,** 487 (1964).
14. T. I. Dyuzheva, S. S. Kabalkina, and L. F. Vereshchagin, *Sov. Phys. Dokl.* **21,** 342 (1976).
15. K.-J. Range, G. H. Grosch, and M. Andratschke, *J. Alloys Comp.* **244,** 170 (1996).
16. N. B. Bolotina, T. I. Dyuzheva, N. A. Bendeliani, V. Petricek, A. E. Petrova, and V. I. Simonov, *J. Alloys Comp.* **278,** 29 (1998).
17. A. P. Hammersley, S. O. Svensson, M. Hanfland, A. N. Fitch, and D. Häusermann, *High Pressure Res.* **14,** 235 (1996).
18. H. K. Mao, J. Xu, and P. M. Bell, *J. Geophys. Res.* **91,** 4673 (1986).
19. A. Boultif and D. Louer, *J. Appl. Crystallogr.* **24,** 987 (1991).
20. A. C. Larson and R. B. von Dreele, "GSAS: General Structure Analysis System", Los Alamos National Laboratory Report LAUR 86-784. 1984.
21. H. Sommer and R. Hoppe, *Z. Anorg. Allg. Chem.* **429,** 118 (1977).
22. P. W. Stephens, *J. Appl. Crystallogr.* **32,** 281 (1999).
23. A. Altomare, M. C. Burla, M. Camalli, B. Carrozzini, G. L. Cascarano, C. Giacovazzo, A. Guagliardi, A. G. G. Moliterni, G. Polidori, and R. Rizzi, *J. Appl. Crystallogr.* **32,** 339 (1999).
24. C. Ritter, E. Gocke, C. Fischer, and R. Schoellhorn, *Mater. Res. Bull.* **27,** 1217 (1992).
25. F. Stewner and R. Hoppe, *Z. Anorg. Allg. Chem.* **374,** 239 (1970).
26. R. Hofmann and R. Hoppe, *Z. Anorg. Allg. Chem.* **555,** 118 (1987).
27. M. Jansen and R. Hoppe, *Z. Anorg. Allg. Chem.* **398,** 54 (1973).
28. W. Bronger, H. J. Miessen, P. Muller, and R. Neugroschel, *J. Less-Common Met.* **105,** 303 (1985).
29. F. Birch, *J. Geophys. Res.* **83,** 1257 (1978).
30. K. Schubert, "Kristallstrukturen zweikomponentiger Phasen." Springer, Berlin, 1964.
31. A. Simon, *Angew. Chem. Int. Ed. Engl.* **20,** 1 (1981).
32. A. Vegas and M. Martínez-Ripoll, *Acta Crystallogr. B* **48,** 747 (1992).